Journal of Materials Chemistry C

ROYAL SOCIETY OF CHEMISTRY

PAPER

View Article Online
View Journal

Cite this: DOI: 10.1039/d5tc01510c

Tuning the band gap and structure from wide gap $SrBi_3O_4Cl_3$ to narrow gap $Bi_4O_4SeCl_2$ by aliovalent anion substitution

T. Robinson,[a] A. Safdar,[a] J. W. Still,[b] I. D. Seymour[a] and Q. D. Gibson *[a]

Received 11th April 2025,
Accepted 7th August 2025

DOI: 10.1039/d5tc01510c

rsc.li/materials-c

Modifying the atomic and electronic structure of materials by chemical substitution is a common method of achieving properties by design. Cations and metal atoms are the most frequent choices for chemical substitution; replacing anions with ones from a different chemical group is unusual due to the very different orbital energies and electronegativities involved. Here we demonstrate full substitution of Se by Cl in the visible band gap material $Bi_4O_4SeCl_2$ charge balanced by simultaneous replacement of Bi with Sr, all the way to the wide gap photocatalyst material $SrBi_3O_4Cl_3$. This compositional flexibility is associated with the layer-segregation of Sr and Se atoms. The crystal structure and electronic structure change non-linearly, with a compositional regime of two band gap transitions observed, due to the introduction of in-gap Se states to the electronic structure. The material $CaBi_3O_4Cl_3$ is also synthesized, revealing the separate effects on the crystal structure of the anion and cation composition. This work presents aliovalent anion substitution in multiple anion materials as a strategy for tuning between narrow and wide gap materials, with properties showing more than one optical transition achievable at intermediate compositions.

Introduction

Multiple anion, or heteroanionic, materials are a class of compounds that have two or more anion species. This chemistry allows for complex packings of the anion sublattices as well as diversity of the chemical bond types compared to single anion materials, facilitating properties such as superconductivity,[1] superionic transport,[2] low thermal conductivity,[3–5] catalysis[6] and quantum magnetism.[7] Properties design *via* chemical tuning of single anion materials often involves either the isovalent or aliovalent substitution of the cation or metal sites, for example tuning the A and B composition in the perovskite structure ABX_3. Isovalent substitution of the anion sites in multiple anion materials can also be utilised, such as band gap tuning in the BiOCl type family for photocatalytic applications[8] or in halide perovskites with photovoltaic applications.[9,10] Aliovalent anion substitution, where an anion is replaced by another anion of a different group, can also be used to tune properties. There are cases in which some O^{2-} replaced by some amount of H^-, F^- or N^{3-}, often charge balanced by a redox active cation becoming reduced or oxidized.[11,12] Another technique is to charge balance aliovalent substitution on the anion sublattice by simultaneous aliovalent substitution on the cation sublattice or of a different anion. For example, Zn_2FN can be synthesized as an analogue to ZnO to tune the band gap and photocatalytic properties,[13] V and O can be simultaneous replaced in $PbVO_2(SeO_3)_2Cl$ and β-$Ba_2[VO_2F_2(IO_3)_2](IO_3)$ by Ga and F to synthesize $PbGaF_2(SeO_3)Cl$[14] and β-$Ba_2[GaF_4(IO_3)_2](IO_3)$[15] to engineer the nonlinear optical properties.

Aliovalent anion substitution in materials allows for a different tuning of properties than either isovalent anion or cation substitution, as materials with different anion groups (*e.g.* halides *vs.* chalcogenides) tend to have very different band gaps and applications due to the large differences in orbital energies in the groups. Full aliovalent substitution, in which an anion is continuously replaced by another is somewhat rare, but has been demonstrated in some zinc blende type photovoltaic materials,[16] with the extreme case of InP-CdS solid solution allowing for band gap tuning from 1.3 eV to 2.6 eV, which occurs in a nonlinear fashion.[17] Tuning the band gap from a narrow band gap (solar absorber) to wide gap (photocatalyst) is of interest, as materials that have intermediate or overlapping properties have unique applications *e.g.* for two photon absorption in photocatalysis and photovoltaics. Aliovalent substitution is a good candidate for this type of materials tuning.

Here we demonstrate full aliovalent substitution of the narrow gap (1.2 eV) layered multiple anion semiconductor $Bi_4O_4SeCl_2$, a natural heterostructure of BiOCl and Bi_2O_2Se

[a] University of Aberdeen, Department of Chemistry, Advanced Centre for Energy and Sustainability (ACES), UK. E-mail: quinn.gibson@abdn.ac.uk
[b] University of Aberdeen, School of Geosciences, UK

with possible solar absorber applications,[18] to the wide gap (2.7 eV) semiconductor $SrBi_3O_4Cl_3$ with applications in catalysis (photocatalytic water splitting[19] and ethane dehydrogenation[20]). Simultaneous Sr^{2+} for Bi^{3+} and Cl^- for Se^{2-} substitution is shown to be possible all the way to the Se^{2-} free compound $SrBi_3O_4Cl_3$. The aliovalent substitution is associated with the layer-segregation of the Se^{2-} and Sr^{2+} ions. Despite the large band gap difference of the two end members (ΔE_G = 1.5 eV), the band gap increases modestly with substitution until compositions where two band gap transitions are observed, allowing for the possibility of two photon absorption. The effect of substitution of the alkali earth on the cation site was also investigated, with synthesis and characterisation of the compound $CaBi_3O_4Cl_3$, demonstrating an increase in band gap and alkali earth independent thickness of the ionic Bi_2O_2Se type layer, indicating that aspects of the structure are primarily dependent on anion composition. The $Bi_4O_4SeCl_2$ structure is therefore open to multiple axes of compositional tuning, establishing a paradigm of aliovalent substitution in multiple anion compounds for materials design.

Experimental section

Synthesis

Compositions of $Sr_xBi_{4-x}O_4Se_{1-x}Cl_{2+x}$ for x = 0, 0.25, 0.5, 0.75, 0.95, 0.99 were synthesized *via* a stochiometric combination of Bi_2O_3, Bi, Se, BiOCl and $SrBiO_2Cl$. Powders were ground in a mortar in pestle, then sealed in an evacuated quartz ampoule at pressures $< 1 \times 10^{-2}$ torr. The ampoules were heated at 700 °C for 12 h in a muffle furnace, then brought to room temperature at 5 °C min^{-1}. The x = 1.0 sample ($SrBi_3O_4Cl_3$) was synthesized through a stochiometric combination of $SrBiO_2Cl$ and BiOCl, ground in a mortar and pestle and heated in an alumina crucible in air at 700 °C. $CaBi_3O_4Cl_3$ was synthesized through a stochiometric combination of $CaBiO_2Cl$ and BiOCl, ground in a mortar and pestle and heated in an alumina crucible in air at 700 °C. The $SrBiO_2Cl$ precursor was synthesized from a stochiometric mixture of $SrCO_3$ and BiOCl, which were ground together in a mortar and pestle, placed in an alumina crucible, and heated in air at 800 °C for 12 h followed by a second identical grinding and heating step. The $CaBiO_2Cl$ precursor was synthesized from a stochiometric mixture of $CaCO_3$ and BiOCl, which were ground together in a mortar and pestle, placed in an alumina crucible, and heated in air at 800 °C for 12 h followed by a two more identical grinding and heating steps.

Powder diffraction measurements were collected on a PANalytical Empyrean powder diffractometer with a Cu Kα tube and a Kα1 monochromator. Data were collected in the range 5° to 120°. Rietveld refinements were performed using GSAS-II.[21]

Diffuse Reflectance measurements were performed on an Agilent Technologies Cary 60 UV-Vis spectrometer with a Harrick Scientific VideoBarrelino Diffuse Reflectance attachment, using $BaSO_4$ as a 100% reflectance background standard. For the plotting of the indirect gap, the background at low energies (between 1.1 and 1.15 eV) was subtracted for better comparison and for extraction of the band gap energy secondary electron microscopy (SEM) and energy dispersive X-ray spectroscopy (EDX) was performed using a Carl Zeiss Gemini SEM 300 with a field emission. EDX was analysed using an Oxford Instruments Aztec Energy EDS analysis system with an XMax 80 detector. The Oxford Instruments Aztec Energy software suite was used for analysis. Samples were coated with 15 nm of carbon prior to measurement to prevent charging. Samples were imaged and analysed using an accelerating voltage of 15 kV.

Density functional theory (DFT) calculations of the energy and electronic structure of $Sr_xBi_{4-x}O_4Se_{1-x}Cl_{2+x}$ and $CaBi_3O_4Cl_3$ compounds were performed using the projector augmented wave (PAW) approach in the VASP code.[22] Non-spin polarised calculations were performed using the Perdew–Burke–Ernzerhof (PBE) functional.[23] Geometry optimisations were performed using a plane-wave cut-off of 520 eV and a gamma centred k-point mesh with a density of $\geq$28 Å.

For the end member $SrBi_3O_4Cl_3$ (x = 1) structure in the $Sr_xBi_{4-x}O_4Se_{1-x}Cl_{2+x}$ series, a single unit cell structure was considered with 50% occupancy of Sr and Bi on the Bi2 site. The same Ca/Bi ordering was used for the $CaBi_3O_4Cl_3$ unit cell structure. For the $Bi_4O_4SeCl_2$ (x = 0) end member, and intermediate $Sr_{0.25}Bi_{3.75}O_4Se_{0.75}Cl_{2.25}$ (x = 0.25) and $Sr_{0.75}Bi_{3.25}O_4Se_{0.25}Cl_{2.75}$ (x = 0.75) systems, a $\sqrt{2} \times \sqrt{2} \times 1$ supercell expansion of the initial unit cell was used to explore different Se/Cl orderings. For the end member $SrBi_3O_4Cl_3$, $Bi_4O_4SeCl_2$ and $CaBi_3O_4Cl_3$ structures, the lattice parameters and atomic positions were optimised until the force on any atom fell below 0.005 eV $Å^{-1}$, with and energy converged of 10^{-7} eV. For intermediate compositions, x = 0.25 and 0.75, the lattice parameters were initially fixed those of the lowest energy x = 0 and x = 1 phases, respectively, and the energies of different Se/Cl orderings were compared, after optimisation of the atomic positions with the same force tolerance of 0.005 eV $Å^{-1}$. The lattice parameters of the lowest energy x = 0.25 and 0.75 structures predicted under fixed cell conditions were then fully optimised before calculation of the electronic structure.

Density of states (DOS) plots were produced for the lowest energy $Sr_xBi_{4-x}O_4Se_{1-x}Cl_{2+x}$ and $CaBi_3O_4Cl_3$ structures using a higher plane wave cut off of 600 eV and a gamma centred k-point mesh with a density of $\geq$56 Å. All DOS plots in this work were visualised in the Sumo package.[24] The formation energy ($E_{form,x}$) per formula unit of the x = 0.25 and 0.75 phases relative to the $Bi_4O_4SeCl_2$ and $SrBi_3O_4Cl_3$ end members was calculated *via* the equation:

$$E_{form,x} = E_x - xE_{SrBi_3O_4Cl_3} - (1-x)E_{Bi_4O_4SeCl_2}$$

where E_x is the energy of the intermediate composition, and $E_{SrBi_3O_4Cl_3}$ and $E_{Bi_4O_4SeCl_2}$ are the energies of the end member phases.

Results and discussion

Composition and structure

All compounds in the series $Sr_xBi_{4-x}O_4Se_{1-x}Cl_{2+x}$ for x = 0, 0.25, 0.5, 0.75, 0.95, 0.99 and 1.0 exhibit X-ray diffraction patterns

consistent with the same *I*4/*mmm* unit cell reported for the $x = 0$ and 1.0 end members ($Bi_4O_4SeCl_2$ and $SrBi_3O_4Cl_3$). SEM-EDX was used to check the actual composition *versus* the nominal value of x. All samples showed small plate-like crystals, as expected from the van der Waals gap containing structure. One key difference is that for $x = 0$, platelike crystals with approximate in plane dimensions of 10 μm were observed (Fig. 1a), whereas for all other compositions, crystallites with in-plane dimensions of one order of magnitude smaller were observed (Fig. 1b). This indicates that that a small change in the components involved in synthesis affects the nucleation and crystal growth kinetics in a way that favours smaller particle sizes in the same experimental conditions. This could be an important consideration when either designing these materials for photovoltaic or photocatalytic applications. The experimental value for x was calculated both from the Se/Cl ratio and the Sr/Bi ratio averaged from 5 measurements for each composition and compared to the nominal value. Fig. 1c shows good agreement between the experimental and nominal values, with the values calculated by Sr/Bi and Se/Cl falling within error of each other and within error of the nominal composition. Along with the preservation of the unit cell, this suggests that the composition was successfully tuned by aliovalent substitution for the series $Sr_xBi_{4-x}O_4Se_{1-x}Cl_{2+x}$. A large uncertainty is observed for $x = 0.25$ likely due to the difficulty of finding sufficiently flat surfaces. It is worth noting that the value for x calculated by the Sr/Bi ratio cannot be less than zero due to zero being the minimum content of Sr, while the value of x calculated by the Se/Cl ratio can go below zero as $x = 0$ corresponds to a ratio of 0.5 Se/Cl. The composition wasn't measured for $x = 0.99$ due to the amount of Se being below the detection limit of the instrument.

All compositions had their lattice parameters and full structure modelled by Rietveld refinements. Fig. 2(a) shows the diffraction patterns for the series and Fig. 2(b) shows an example Rietveld refinement for $x = 0.75$. Full Rietveld refinements for the whole series are shown in the SI. The diffraction patterns show the same *I*4/*mmm* pattern for every x, with small shifts in the lattice parameters observable. For $x = 0$, peaks containing a non-zero l index are more than for any other in the series, due to significant preferred orientation in the $x = 0$ particles

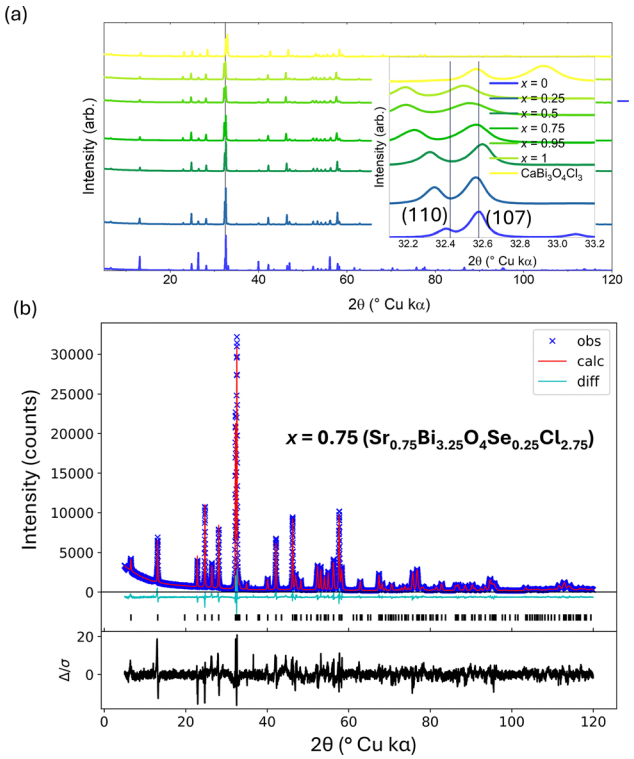

Fig. 2 (a) Diffraction patterns for the series $Sr_xBi_{4-x}O_4Se_{1-x}Cl_{2+x}$. x =0.99 was omitted due to its similarity $x = 1.0$ Patterns are offset from each other for better visibility. Inset: A close up of the (110) and (107) pair of peaks, showing peak shift as a function of x as well as the shift towards higher angle for $CaBi_3O_4Cl_3$ compared to all Sr containing materials. (b) Example Rietveld refinement for $x = 0.75$ ($Sr_{0.75}Bi_{3.25}O_4Se_{0.25}Cl_{2.75}$), with a $\chi^2 = 5.65$, an $R_W = 8.24\%$ and goodness of fit = 2.37.

from the particle morphology (Fig. S1–S6, S15 and S16). The apparent broadening of the (107) peak with Sr incorporation in Fig. 2(a) is actually an artefact of this preferred orientation, as demonstrated by comparing the (002) and (200) peaks across the series (Fig. S15 and S16); no evidence of significant inhomogeneity-based broadening was observed in this solid solution.

Fig. 3 shows the full modelled structure for the series as determined by Rietveld refinements of powder XRD data.

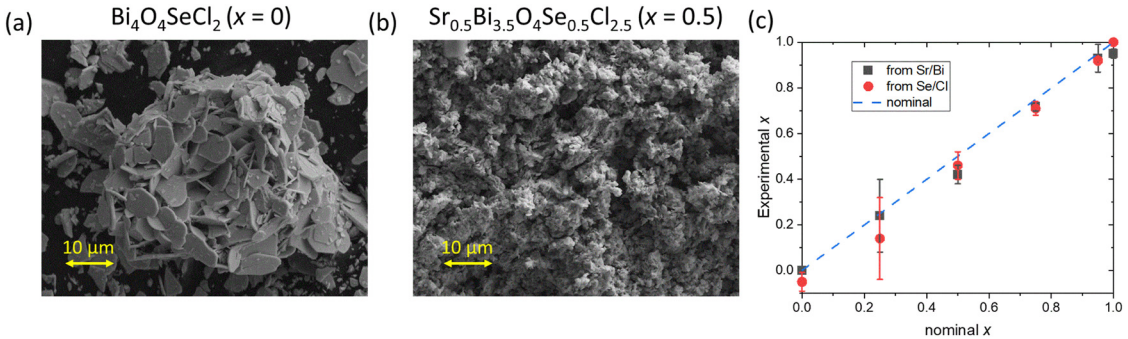

Fig. 1 SEM images for (a) $x = 0$ $Bi_4O_4SeCl_2$ and (b) $Sr_{0.5}Bi_{3.5}O_4Se_{0.5}Cl_{2.5}$ on the same scale, demonstrating the difference in particle size. (c) comparison of the value for x calculated by the Sr/Bi ratio and Se/Cl ratio as determined by EDX to the nominal value of x. The dashed line shows the expected trend if the experimental equals the nominal.

Compositions were constrained to the nominal composition due to the agreement of the nominal and experimental compositions shown in Fig. 1(b). The structure of the series overall is defined by Bi_2O_2 fluorite type layers separated alternatively by a ionic bridging layer (Se1/Cl1) and a van der Waals layer (Se2/Cl2). Refining the Sr occupancy on both the Bi1 (adjacent to the ionic bridging layer) and Bi2 (adjacent to the van der Waals layer) sites in the Bi_2O_2 demonstrated that within error, all Sr occupies the Bi2 position at every composition, consistent with the reported structure for $SrBi_3O_4Cl_3$. For x = 0, the Se is distributed both across the ionic bridging layer and van der Waals layer, with a statistical site preference for the ionic bridging layer. Upon Sr substitution, this site preference gets more marked; at compositions of x = 0.75 and larger, Se only occupies the ionic bridging layer to within error of the model, refining to a slightly negative value when freely refined, though a small amount of Se on the Se2 site cannot be ruled out.

Lattice parameter trends are shown in Fig. 4(a). The in-plane lattice parameter a varies linearly with x across the series, consistent with Vegard's law and the larger size of Sr^{2+} compared to Bi^{3+}. By contrast, the lattice parameter c varies non-monotonically with x. The c lattice parameter depends on the thickness of the ionic bridging layer, the van der Waals layer and the Bi_2O_2 fluorite type layer. These layers are being affected simultaneously in different ways, with the total amount of Se being less with x, the site preference of Se for the Se1 site increasing with x and the amount of Sr increasing on the Bi2 site. The site preference can be seen when the ratio of the occupancy of Se in the Se2 site *versus* the Se1 site is plotted as a function of x in Fig. 4(b). A quick drop off is observed around x = 0.5, after which, within uncertainty of modelling the diffraction data, all the Se occupies the Se1 site. Therefore, the amount of Se in the Se1 site is not directly proportional to x. The effect of this on the lattice parameter c can be seen when plotting the thickness of the ionic bridging layer, as defined by the cross-plane Bi1–Bi1 distance (Fig. 4(c)). This value changes monotonically but not linearly with x. By instead plotting it is a function of the occupancy of Se in the Se1 site, x_{Se1}, a linear trend is observed (Fig. 4(d)). Indeed, this layer thickness for $CaBi_3O_4Cl_3$ fits on this linear trend as well, despite the smaller overall c lattice parameter of $CaBi_3O_4Cl_3$ compared to $SrBi_3O_4Cl_3$ (26.6398(5) Å and 26.9997(4) Å respectively). This demonstrates that the thickness of the ionic bridging layer is dependent only on the anion composition at the bridging site, a consequence of the tendency of the alkali earth to only sit at the Bi2 site. The smaller c axis of $CaBi_3O_4Cl_3$ compared to $SrBi_3O_4Cl_3$ is therefore related to a contraction of the Bi_2O_2 and van der Waals layers due to the smaller Ca^{2+} cation. The ionic bridging layer can therefore be tuned by the anion composition at the bridging site, and the other layers tuned by choice of alkali earth, allowing for different compositional degrees of freedom for modifying the layer thicknesses at different points in the structure. Given the importance of these layers for *e.g.* thermal conductivity, the ability to tune the bonding at each layer in this type of natural heterostructure could be another method of introducing phonon engineering.

That the presence of Sr on the Bi2 site increases the site preference of Se for the Se1 site is consistent with electrostatics. A lower Coulomb energy is achieved by Se^{2-} having Bi^{3+} for its nearest neighbours, and Sr^{2+} with Cl^- than compared with the converse. Thus the confinement of Sr^{2+} to the layer defined by the Bi2 site leads to the confinement of the Se^{2-} to the layer defined by the Bi1 site. The effect of doping on the structure is therefore nontrivial as the Sr and Se occupancies are correlated.

Band gaps and electronic structure

The band gaps were measured *via* diffuse reflectance UV-Vis spectroscopy on powders of samples for the series $Sr_xBi_{4-x}O_4Se_{1-x}Cl_{2+x}$ and $CaBi_3O_4Cl_3$. Fig. 5(a) and (b) show Tauc plots as a function of x for the direct and indirect gap respectively. For the values of x = 0.75, x = 0.95 and x = 0.99 two onset features

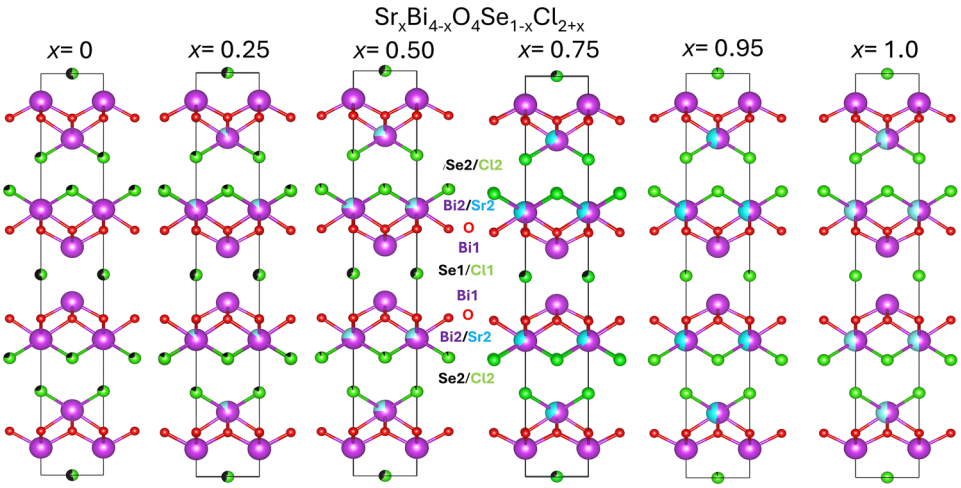

Fig. 3 Crystal structures of $Sr_xBi_{4-x}O_4Se_{1-x}Cl_{2+x}$ for x = 0, 0.25, 0.50, 0.75, 0.95 and 1.0 as modelled by Rietveld refinements from powder data. Partial occupancies are shown by a partial colouring in of an atomic site.

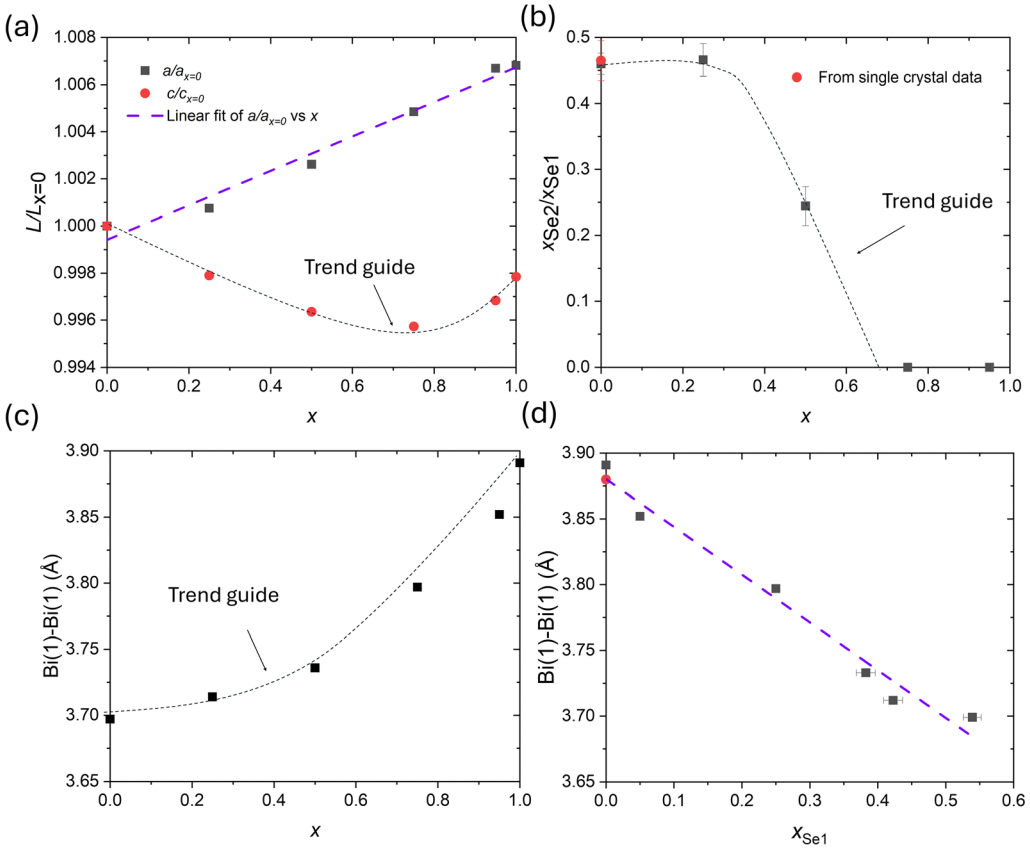

Fig. 4 (a) lattice parameter trends for a (black) and c (red) as a function of x in $Sr_xBi_{4-x}O_4Se_{1-x}Cl_{2+x}$. A linear fit is shown for a and a trend guide line is shown for c. (b) ratio of Se on the Se2 site to the Se1 site as a function of x in $Sr_xBi_{4-x}O_4Se_{1-x}Cl_{2+x}$. A trend guide line is shown as a dashed line. The red point is the ratio from published crystal structure determined from single crystal diffraction in ref. 18. This value and the corresponding value modelled by powder data here are within error of each other, 0.47(3) and 0.46(2) respectively. (c) the thickness of the bridging ionic layer, as defined by the Bi1–Bi1 distance as a function of $Sr_xBi_{4-x}O_4Se_{1-x}Cl_{2+x}$ and (d) as a function of x_{Se1} (the Se occupancy of the Se1 site). For (c) a trend guide line is shown, and for (d) a linear fit is shown. The data point for $CaBi_3O_4Cl_3$ is shown in red in (d). For all plots, where error bars are not visible, they are smaller than the size of the data points.

are observed in different energy ranges; these were extracted as E_G direct, E_G indirect, E_G direct 2 and E_G indirect 2. The observation of two transitions for x = 0.75, x = 0.95 and x = 0.99 is of particular interest due to the application of $SrBi_3O_4Cl_3$, in photocatalysis. $SrBi_3O_4Cl_3$, is a known photocatalyst, the introduction of in-gap states with Se addition may allow for two-photon absorption processes that allow for photocatalytic activities across a broader spectrum of incident light.

A clear shift towards higher energies can also be observed as a function of x. Fig. 5(a) and (b) show the extracted band gap as a function of x. There is a monotonic, linear increase in both the direct and indirect gaps from x = 0 to x = 0.75, with the direct gap increasing by 0.25 eV and the indirect gap increasing by 0.20 eV. Above x = 0.75, this linear relationship breaks down, with the indirect gap decreasing to lower values for x = 0.95 and x = 0.99. At the same time, the band gap associated with the second transition approaches the value observed for x = 1.0 ($SrBi_3O_4Cl_3$). For x = 0.99, the higher energy band gaps are within error of that of $SrBi_3O_4Cl_3$, and that the indirect and direct gaps for the smaller energy transition are within error of each other. This supports a picture of a localised defect-like Se state 1.36(8) eV below the conduction band minimum for x = 0.99. The overall trends are consistent with the introduction of a semi-isolated Se p band upon introduction of Se into $SrBi_3O_4Cl_3$, which has poor orbital mixing with the O and Cl p states, as corroborated by density of states calculations (Fig. 6). The linear relationship in gap between from x = 0 and x = 0.75 is evidence of some orbital mixng, however the very modest change (0.2 eV) given the large difference in band gap between x = 0 and x = 1.0 is evidence that this orbital mixing is weak. This is because the Se p states sit at considerably higher energy than the Cl or O p states.

In the DOS calculations (Fig. 6), for the $SrBi_3O_4Cl_3$ (x = 1) end member, the top of the valence band is primarily of O 2p character, and the bottom of the conduction band is dominated by Bi 6p states. The energy gap between the valence and conduction band predicted by DFT is 1.60 eV, which is smaller than the experimentally observed indirect gap for $SrBi_3O_4Cl_3$ of 2.58 eV. The PBE functional used in this work is well known to lead to an underestimate of experimentally observed band gaps but allows for a qualitative comparison with other compounds in the series. As Se is introduced into the structure to

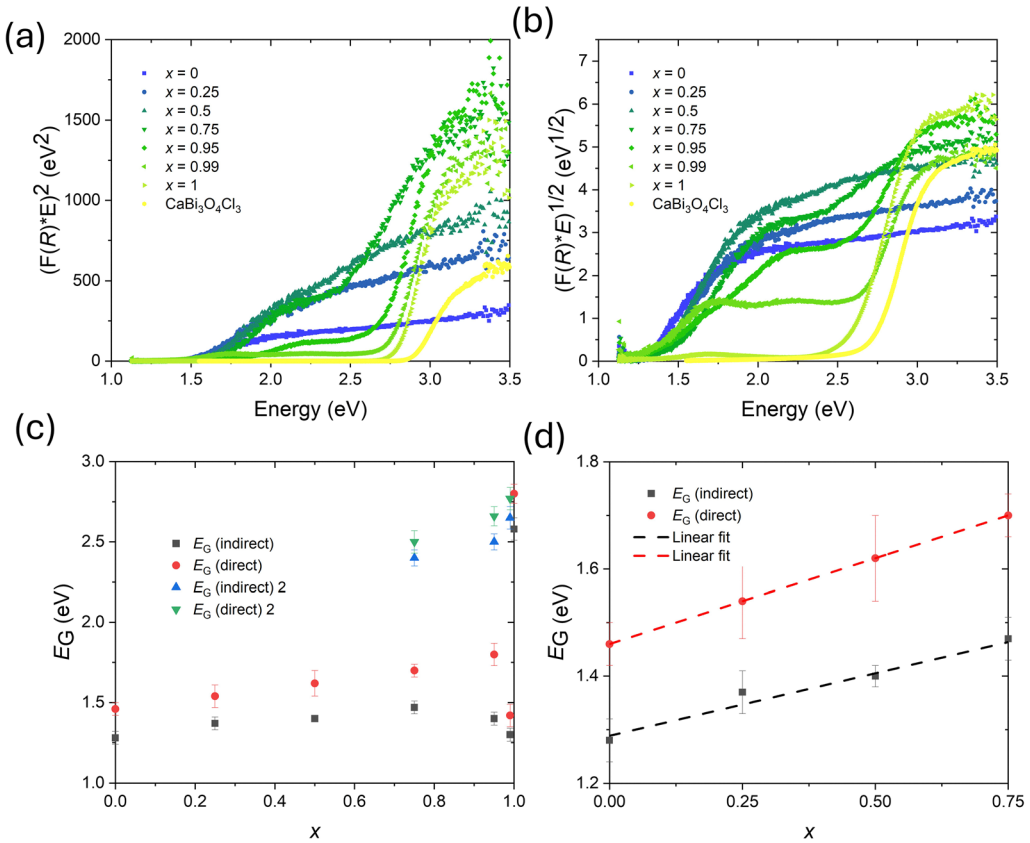

Fig. 5 (a) Tauc plot for the direct band gap from diffuse reflectance data for the series $Sr_xBi_{4-x}O_4Se_{1-x}Cl_{2+x}$ and $CaBi_3O_4Cl_3$ (b) Tauc plot for the indirect band gap from diffuse reflectance data for the series $Sr_xBi_{4-x}O_4Se_{1-x}Cl_{2+x}$ (c) Extracted indirect and direct band gap energies for the series $Sr_xBi_{4-x}O_4Se_{1-x}Cl_{2+x}$. x = 0.75, x = 0.95 and x = 0.99 display two onset features in different energy ranges; these were extracted as E_G direct, E_G indirect, E_G direct 2 and E_G indirect 2. An example of how the band gap values and uncertainties were extracted is shown in Fig. S18.

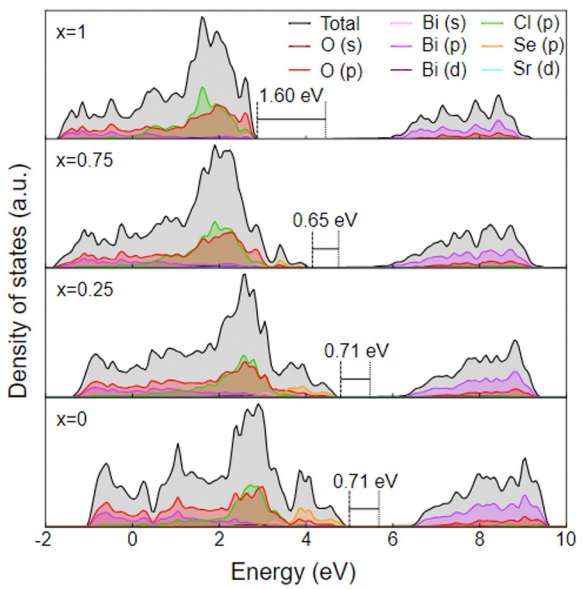

Fig. 6 Density of states plots for low energy $Sr_xBi_{4-x}O_4Se_{1-x}Cl_{2+x}$ structures. Positions of valence band maximum and conduction band minimum are shown for each system as dashed and dotted lines, respectively, with the corresponding energy gap in eV. Zoom-ins around the Fermi energy are shown in Fig. S19.

$Sr_{0.75}Bi_{3.25}O_4Se_{0.25}Cl_{2.75}$ (x = 0.75), the valence band becomes dominated by Se 4p states whereas there is little change to the character of the conduction band. The introduction of the Se 4p states results in a significant reduction in the PBE energy gap to 0.65 eV. This 0.95 eV drop in the band gap as Se is introduced into the structure is consistent with the experimental measurements, which demonstrate a drop from 2.58 eV at x = 1 to 1.47 eV for x = 0.75, or a 1.11 eV drop. As the fraction of Se increases in the structure, the number of Se states at the valence band edge increases, but there is only a small change in the energy gap from x = 0.75 to x = 0, again consistent with the only modest change in band gap observed experimentally across this range. In experiment, the band gap will be modified slightly by disorder, as orderings other than the lowest energy one are accessible as demonstrated by a lack of superstructure ordering and Se occupation of both anion sites observed across the series. Overall, the computational and experimental results support the interpretation of a semi-isolated Se state being introduced in the band gap, where its DOS and bandwidth depend on the amount of Se introduced into the system. The separated Se orbital manifold in the x = 0.75 supports the interpretation of a likely isolated Se orbital manifold in the x = 0.95 and x = 0.99 compositions; however, there is some level of Se–O hybridization in the in-gap states that must be

taken into account, as evidenced by the non-trivial O contribution to the in-gap Se states.

The effect of the alkali earth is seen when comparing the band gaps of $SrBi_3O_4Cl_3$ with $CaBi_3O_4Cl_3$, which are both indirect and 2.58(7) eV and 2.72(8) eV respectively (Fig. S14). The direct gaps are 2.80(6) and 2.90(4) eV respectively as well. In the DOS calculations (Fig. S15), when Sr is swapped for Ca, the computed energy gap increases from 1.60 to 1.67 eV, an increase that is within error of the experimentally observed increase. In both structures, the valence band edge is dominated by O 2p states and the conduction band by Bi 6p states. The increase in the gap from Sr to Ca is primarily related to the increase in the ionicity of the latter cation. This demonstrates the alkali earth cation to be a minor but independent source of tuning the electronic structure in this series; replacing Sr with the smaller and less electropositive Ca leads to a larger band gap allowing for another mechanism to tune the band gap in this structure type.

Overall, the results presented here differentiate this aliovalent anionic substitution from the usual isovalent substitution; by going from one group to another, the energy difference in the orbital energy levels is increased more than by going from *e.g.* Cl to Br to I. For example, the band gap difference between Bi_2O_2Se (0.8 eV)[25] and BiOCl (3.5 eV)[26] is much larger than the difference between BiOCl (3.5 eV) and BiOBr (2.9 eV).[27] Thus, aliovalent anion substitution has qualitatively different effects on the electronic structure compared with isovalent anion substitution. The ability to synthesize this series demonstrate that $Bi_4O_4SeCl_2$ has significant compositional and structural flexibility, with full aliovalent substitution possible all the way up to $SrBi_3O_4Cl_3$, and substitution of Ca possible for Sr. The existence of photocatalytic $PbBi_3O_4Cl_3$[28] as well as analogous bromides and other stacking homologues such as $Bi_6O_6Se_2Cl_2$[29,30] indicates that the level of tunability in terms of compositions and properties in this family of multiple anion and layered materials is vast, providing an alternative paradigm for properties design by anion substitution. A generalised formula can be written as $A_xBi_{2+2n-x}O_{2+2n}Se_{n-x}X_{2+x}$ where A = (Ca, Sr, Pb) and X = (Cl, Br). It is also worth investigating if $Bi_4O_4SeCl_2$ can be doped aliovalently in the other direction, *e.g.* $M_xBi_{4-x}O_4Se_{1+x}Cl_{2-x}$ where M is a tetravalent element such as Zr, Hf or possibly Ge/Sn.

Conclusions

Two materials with similar structures but differing band gaps, $SrBi_3O_4Cl_3$ and $Bi_4O_4SeCl_2$, can be tuned between each other across the complex solid solution series $Sr_xBi_{4-x}O_4Se_{1-x}Cl_{2+x}$. Further, the alkali earth cation can be replaced by Ca, demonstrating this family of multiple anion Bi-based layered materials to exhibit a large amount of chemical flexibility. Due to the very different electronegativities, any amount of Se for Cl substitution leads to a collapse of the band gap by about 1.2 eV, and at small amounts of Se, two band-gap type transitions are observed in the diffuse reflectance. At larger amounts of Se, a small but linear change in band gap is observed with composition. The structure behaves as more complex than a typical solid solution, with the presence of Sr affecting the distribution of Se across the anion sites. Overall, these results demonstrate that aliovalent anion substitution can be done across a wide range of composition for multiple anion layered materials, and leads to a tuning of the electronic structure and crystal structure that is complex but still follows chemical rules, leading to different types of properties from either aliovalent cation substitution or isovalent anion substitution. Aliovalent anion substitution is therefore a complementary approach to structural and electronic tuning, particularly in layered multiple anion solids.

Conflicts of interest

There are no conflicts to declare.

Data availability

Data has been made available as SI.

The supporting information contains four sections: (1) secondary electron microscopy (SEM) and energy dispersive X-ray spectroscopy (EDX). (2) Powder diffraction and Rietveld refinements. (3) Diffuse reflectance. (4) Density dunctional theory calculations. Crystallographic information files for all compounds for which Rietveld refinements were performed are also included as SI. See DOI: **https://doi.org/10.1039/d5tc01510c**.

Acknowledgements

I. D. S. would like to acknowledge support from his UKRI Future Leaders Fellowship (MR/Y018222/1).

References

1 H. Takahashi, K. Igawa, K. Arii, Y. Kamihara, M. Hirano and H. Hosono, Superconductivity at 43 K in an Iron-Based Layered Compound $LaO_{1-x}F_xFeAs$, *Nature*, 2008, **453**(7193), 376–378.

2 G. Han, A. Vasylenko, L. M. Daniels, C. M. Collins, L. Corti, R. Chen, H. Niu, T. D. Manning, D. Antypov, M. S. Dyer, J. Lim, M. Zanella, M. Sonni, M. Bahri, H. Jo, Y. Dang, C. M. Robertson, F. Blanc, L. J. Hardwick, N. D. Browning, J. B. Claridge and M. J. Rosseinsky, Superionic Lithium Transport via Multiple Coordination Environments Defined by Two-Anion Packing, *Science*, 2024, **383**(6684), 739–745.

3 Q. D. Gibson, T. Zhao, L. M. Daniels, H. C. Walker, R. Daou, S. Hébert, M. Zanella, M. S. Dyer, J. B. Claridge, B. Slater, M. W. Gaultois, F. Corà, J. Alaria and M. J. Rosseinsky, Low Thermal Conductivity in a Modular Inorganic Material with Bonding Anisotropy and Mismatch, *Science*, 2021, **373**(6558), 1017–1022.

4 C. J. Hawkins, J. A. Newnham, B. Almoussawi, N. L. Gulay, S. L. Goodwin, M. Zanella, T. D. Manning, L. M. Daniels,

M. S. Dyer, T. D. Veal, J. B. Claridge and M. J. Rosseinsky, Synthesis, Structure, and Properties of $CuBiSeCl_2$: A Chalcohalide Material with Low Thermal Conductivity, *Chem. Mater.*, 2024, **36**(9), 4530–4541.

5 J. M. Hodges, Y. Xia, C. D. Malliakas, G. C. B. Alexander, M. K. Y. Chan and M. G. Kanatzidis, Two-Dimensional $CsAg_5Te_{3-x}S_x$ Semiconductors: Multi-Anion Chalcogenides with Dynamic Disorder and Ultralow Thermal Conductivity, *Chem. Mater.*, 2018, **30**(20), 7245–7254.

6 J. M. Thomas, W. Ueda, J. Williams and K. D. M. Harris, New Families of Catalysts for the Selective Oxidation of Methane, *Faraday Discuss. Chem. Soc.*, 1989, **87**, 33–45.

7 D. Hirai, Pinalites: Optical Properties and Quantum Magnetism of Heteroanionic $A_3MO_5X_2$ Compounds, *Inorg. Chem.*, 2024, 4001–4010.

8 Y. Liu, W. J. Son, J. Lu, B. Huang, Y. Dai and M. H. Whangbo, Composition Dependence of the Photocatalytic Activities of $BiOCl_{1-x}Br_x$ Solid Solutions under Visible Light, *Chem. – Eur. J.*, 2011, **17**(34), 9342–9349.

9 Z. Wang, Z. Shi, T. Li, Y. Chen and W. Huang, Stabilität von Perowskit-Solarzellen: Einfluss Der Substitution von A-Kation Und X-Anion, *Angew. Chem.*, 2017, **129**(5), 1210–1233.

10 H. M. Ghaithan, S. M. H. Qaid, Z. A. Alahmed, M. Hezam, A. Lyras, M. Amer and A. S. Aldwayyan, Anion Substitution Effects on the Structural, Electronic, and Optical Properties of Inorganic $CsPb(I_{1-x}Br_x)_3$ and $CsPb(Br_{1-x}Cl_x)_3$ Perovskites: Theoretical and Experimental Approaches, *J. Phys. Chem. C*, 2021, **125**(1), 886–897.

11 H. Kageyama, K. Hayashi, K. Maeda, J. P. Attfield, Z. Hiroi, J. M. Rondinelli and K. R. Poeppelmeier, Expanding Frontiers in Materials Chemistry and Physics with Multiple Anions, *Nat. Commun.*, 2018, **9**(1), 772.

12 N. Charles, R. J. Saballos and J. M. Rondinelli, Structural Diversity from Anion Order in Heteroanionic Materials, *Chem. Mater.*, 2018, **30**(10), 3528–3537.

13 S. R. Lingampalli, K. Manjunath, S. Shenoy, U. V. Waghmare and C. N. R. Rao, Zn_2NF and Related Analogues of ZnO, *J. Am. Chem. Soc.*, 2016, **138**(26), 8228–8234.

14 F. You, F. Liang, Q. Huang, Z. Hu, Y. Wu and Z. Lin, $Pb_2GaF_2(SeO_3)_2Cl$: Band Engineering Strategy by Aliovalent Substitution for Enlarging Bandgap While Keeping Strong Second Harmonic Generation Response, *J. Am. Chem. Soc.*, 2019, **141**(2), 748–752.

15 J. Chen, C. Hu, F. Mao, J. Feng and J. Mao, A Facile Route to Nonlinear Optical Materials: Three-Site Aliovalent Substitution Involving One Cation and Two Anions, *Angew. Chem.*, 2019, **131**(7), 2120–2124.

16 W. Yang, B. Liu, B. Yang, J. Wang, T. Sekiguchi, S. Thorsten and X. Jiang, Pseudobinary Solid-Solution: An Alternative Way for the Bandgap Engineering of Semiconductor Nanowires in the Case of GaP-ZnSe, *Adv. Funct. Mater.*, 2015, **25**(17), 2543–2551.

17 M. Glicksman and W. D. Kraeft, Effect of High Intrinsic Ion Concentrations on Electron Energies in Solid Solutions of III-V and II-VI Semiconductors, *Solid State Electronics*, 1985, **28**(1–2), 151–161.

18 Q. D. Gibson, T. D. Manning, M. Zanella, T. Zhao, P. A. E. Murgatroyd, C. M. Robertson, L. A. H. Jones, F. McBride, R. Raval, F. Cora, B. Slater, J. B. Claridge, V. R. Dhanak, M. S. Dyer, J. Alaria and M. J. Rosseinsky, Modular Design via Multiple Anion Chemistry of the High Mobility van der Waals Semiconductor $Bi_4O_4SeCl_2$, *J. Am. Chem. Soc.*, 2020, **142**(2), 847–856.

19 H. Suzuki, D. Ozaki, Y. Ishii, O. Tomita, D. Kato, S. Nozawa, K. Nakashima, A. Saeki, H. Kageyama and R. Abe, A Sillén Oxyhalide $SrBi_3O_4Cl_3$ as a Promising Photocatalyst for Water Splitting: Impact of the Asymmetric Structure on Light Absorption and Charge Carrier Dynamics, *J. Mater. Chem. A*, 2023, **11**(28), 15159–15167.

20 W. Ueda, S.-W. Lin and I. Tohmoto, Highly Selective Oxidative Dehydrogenation of Ethane to Ethene over Layered Complex Metal Chloride Oxide Catalysts, *Catal. Lett.*, 1997, **44**, 241–245.

21 B. H. Toby and R. B. Von Dreele, GSAS-II: The Genesis of a Modern Open-Source All Purpose Crystallography Software Package, *J. Appl. Crystallogr.*, 2013, **46**(2), 544–549.

22 G. Kresse and D. Joubert, From Ultrasoft Pseudopotentials to the Projector Augmented-Wave Method, *Phys. Rev. B: Condens. Matter Mater. Phys.*, 1999, **9**(3), 1758.

23 J. P. Perdew, K. Burke and M. Ernzerhof, Generalized Gradient Approximation Made Simple, *Phys. Rev. Lett.*, 1996, **77**(18), 3865.

24 M. Ganose, A. J. Jackson, A. O. Scanlon and D. Sumo, Command-Line Tools for Plotting and Analysis of Periodic Ab Initio Calculations, *J. Open Source Software*, 2018, **3**(28), 717.

25 Y. Sun, J. Zhang, S. Ye, J. Song and J. Qu, Progress Report on Property, Preparation, and Application of Bi_2O_2Se, *Adv. Func. Mater.*, 2020, **30**(49), 2004480.

26 D. Cui, L. Wang, K. Xu, L. Ren, L. Weng, Y. Yu, Y. Du and W. Hao, Band-Gap Engineering of BiOCl with Oxygen Vacancies for Efficient Photooxidation Properties under Visible-Light Irradiation, *J. Mater. Chem. A*, 2018, **6**(5), 2193–2199.

27 Y. Wang, Z. Shi, C. Fan, X. Wang, X. Hao and Y. Chi, Synthesis, Characterization, and Photocatalytic Properties of BiOBr Catalyst, *J. Solid State Chem.*, 2013, **199**, 224–229.

28 H. Suzuki, M. Higashi, O. Tomita, Y. Ishii, T. Yamamoto, D. Kato, T. Kotani, D. Ozaki, S. Nozawa, K. Nakashima, K. Fujita, A. Saeki, H. Kageyama and R. Abe, $PbBi_3O_4X_3$ (X = Cl, Br) with Single/Double Halogen Layers as a Photocatalyst for Visible-Light-Driven Water Splitting: Impact of a Halogen Layer on the Band Structure and Stability, *Chem. Mater.*, 2021, **33**(24), 9580–9587.

29 R. Ji, M. Lei, C. Genevois, W. Zhang, X. Ming, L. He, M. Allix, C. Yin, X. Kuang and X. Xing, Multiple Anion Chemistry for Ionic Layer Thickness Tailoring in $Bi_{2+2n}O_{2+2n}Se_nX_2$ (X = Cl, Br) van der Waals Semiconductors with Low Thermal Conductivities, *Chem. Mater.*, 2022, **34**(10), 4751–4764.

30 Q. D. Gibson, J. A. Newnham, M. S. Dyer, C. M. Robertson, M. Zanella, T. W. Surta, L. M. Daniels, J. Alaria, J. B. Claridge and M. J. Rosseinsky, Expanding Multiple Anion Superlattice Chemistry: Synthesis, Structure and Properties of $Bi_4O_4SeBr_2$ and $Bi_6O_6Se_2Cl_2$, *J. Solid State Chem.*, 2022, **312**, 123246.

